

Dynamic communication between androgen and coactivator: Mutually induced conformational perturbations in androgen receptor ligand-binding domain

Xue Xu,^{1,2,3} Wei Yang,^{1,2,3} Xia Wang,^{1,2} Yan Li,³ Yonghua Wang,^{1,2*} and Chunzhi Ai⁴

¹ College of Life Science, Northwest A & F University, Yangling 712100, Shaanxi, China

² Center of Bioinformatics, Northwest A & F University, Yangling 712100, Shaanxi, China

³ School of Chemical Engineering, Dalian University of Technology, Dalian 116012, Liaoning, China

⁴ Lab of Pharmaceutical Resource Discovery, Dalian Institute of Chemical Physics,

The Graduate School of Chinese Academy of Sciences, Dalian 116023, Liaoning, China

ABSTRACT

The transcriptional activity of androgen receptor (AR) is regulated by the sequential binding of various ligands (e.g., dihydrotestosterone, DHT) and coactivators (e.g., SRC/p160) to the AR ligand binding domain (LBD) (Askew et al., *J Biol Chem* 2007;282:25801–25816, Lee and Chang, *Cell Mol Life Sci* 2003;60:1613–1622). However, the synergism between the recruitments of coactivator (SRC 2–3) and ligand (such as DHT) to AR at atomic level remains unclear. Thus, in this work, extensive explicit-solvent molecular dynamics (MD) simulations on four independent trajectories, that is, AR-apo (unbound), DHT-AR, AR-SRC, and DHT-AR-SRC, are performed to investigate the potential communications between the two events in the AR transcriptional process. The MD simulations, analysis of the dynamical cross-correlation maps, comparisons of the binding energy, and thermodynamic analysis reveal a definite structural and functional link between Activation Function-2 (AF-2) surface and the ligand binding site influenced by the binding of ligand and coactivator to the LBD: (I) The DHT binding can increase the LBD volume to 753.0 Å³ from its compact ligand-free state (372.1 Å³), resulting in a group of helices (1, 2, 8, and loop 2') to move outward and exert added traction on the ligand binding pathway, which subsequently leads to rearrange the AF-2 region to well recruit the SRC; (II) Similarly, the SRC recruitment is also found to facilitate the ligand binding through transmitting a concomitant push-pull effort from the AF-2 surface to the DHT binding site, leading to the opening of entrance to the LBD formed by Val684, Met745, and Arg752, increase of the volume of binding pocket (896.4 Å³) and stabilization of the dynamic structure of the LBD. These results, in a dynamic form, initially show a bidirectional structural and functional relay between the bound DHT and SRC that establishes AR functional potency.

Proteins 2011; 79:1154–1171.
© 2010 Wiley-Liss, Inc.

Key words: androgen receptor; dynamic communication; dihydrotestosterone; coactivator; molecular dynamics; thermodynamic analysis.

INTRODUCTION

The nuclear hormone receptor (NR) gene family represents a class of 48 known transcription factors that modulate hormone-dependent gene expression¹ and increase gene activity by recruiting coregulators that assist in chromatin remodeling.² The nuclear receptors are broadly implicated in normal physiological development and metabolism and represent therapeutic targets for a wide range of human diseases, including cancer, endocrine, metabolic disorders, and heart diseases.^{3,4} Thus, androgen receptor (AR), a member of the nuclear receptor superfamily, becomes one of the major targets for pharmaceutical development and a recognized target for existing prostate cancer therapies, including androgen withdrawal and anti-androgens.^{5,6}

Recent models of AR action suggest that AR transcription function stems from potent hormone-independent activation function 1 (AF-1), and emphasize the role of contacts between the LXXLL motifs (where L is leucine and X is any amino acid) and the second activation function (AF-2) in the ligand-binding domain (LBD).⁷ AF-1 in the NH₂-terminal region is the major transactivation domain with a receptor and cell-type dependent activity.¹ AF-2 is a highly conserved

Additional Supporting Information may be found in the online version of this article.

Grant sponsor: National Natural Science Foundation of China; Grant number: 10801025; Grant sponsor: The Fund of Northwest A & F University; The research is supported by high-performance computing platform of Northwest A & F University.

Xue Xu, Wei Yang, and Yan Li contributed equally to this work.

*Correspondence to: Yonghua Wang, Center of Bioinformatics, Northwest A & F University, Yangling 712100, Shaanxi, China. E-mail: yh_wang@nwsuaf.edu.cn.

Received 24 August 2010; Revised 9 October 2010; Accepted 16 November 2010
Published online 30 November 2010 in Wiley Online Library (wileyonlinelibrary.com). DOI: 10.1002/prot.22951

hydrophobic surface formed by helices 3, 3', 4, and 12 and is flanked by clusters of oppositely charged residues.¹ This region is stabilized by agonists [e.g., testosterone (T) and dihydrotestosterone (DHT)] binding, and binds to coregulators via the short leucine-rich hydrophobic motifs (NR boxes, consensus LXXLL motifs) reiterated within each steroid receptor coactivator (SRC), in which the leucine residues dock into the hydrophobic cleft.⁸ Although the AR AF-2 contacts with the LXXLL motifs are weak, several lines of evidence propose that the mutation of AR coactivators inhibits the AR coactivation, while not significantly affects the ligand binding,⁹ showing that AF-2 contributes directly to the coactivator recruitment in some contexts.

Beneath the exposed surface of the AR AF-2 coactivator-binding region is a shallow interface juxtaposed against the ligand binding pocket. This close structural arrangement provides a platform for the potential communication between AF-2 and the bound ligand in regulating the AR transcriptional activity.^{5,10} Some experimental evidence has already shown that the AR binding of the biologically active androgens T and DHT might stabilize the AF-2 binding surface^{11,12} and facilitate the interactions of the receptor with the coactivator. This might partially explain the long-standing mystery why high-affinity ligands induce low levels of transcription, as they presumably elicit a conformation of the AR AF-2 that is suboptimal for the coactivator recruitment.¹

Further, it has been suggested that the AF-2 activation is determined by the equilibrium of different conformations of the helix 12 and that a ligand does not usually induce one static conformation, but rather changes the equilibrium toward more active conformations in the case of agonists or toward inactive conformations in the case of antagonists.¹³ The positioning of helix 12 is crucial for the receptor activation as indicated by its structural data, together with transcriptional activation data.^{2,7} Previous experimental studies have proposed that the conformation of helix 12, forming one side of the AF-2 surface by docking against helices 3 and 11 in the presence of agonist ligands, is folded up against the core, creating a lid over the ligand-binding pocket.¹² Evidently, the conformational arrangement of the binding pocket can be propagated to the AF-2 region of the protein complexes thus impacting the coactivator binding kinetics. On the other hand, the functional link between AF-2 and the ligand-binding pocket is also supported by the evidence that mutation of the AF-2 domain dramatically influences the transcriptional activation in response to ligand, that is, somatic AR mutations in AF-2 increase the androgen dissociation and increase the AR stabilization and the coactivator recruitment.¹⁴ It is worthy of noting that the ligand activation of transcription involves a formation of the AF-2 surface by folding the carboxyl-terminal helix 12 against a scaffold of helices 3, 3', 4. But until recently, the dynamics interactions between the ligand binding region and AF-2 still remain elusive. More-

over, the static LBD crystal structures of ligand-bound AR LBDs in complex with several FXXLF and LXXLL peptide motifs (where F is phenylalanine, L is leucine, and X is any amino acid) only provide subtle clues how these ligands and coactivators transmit different signals to the LBDs. The above observations, naturally, raise some questions concerning with the dynamic effects of the DHT/SRC binding on the AR protein, that is,

1. How do local motions of the helices in response to the ligand binding propagate to influence the conformational change of AF-2 region;
2. What dynamics results in the folding/unfolding of helices residing in the neighboring of the AF-2 activation domain;
3. What is the functional role of SRC recruitment in its communication with the structural arrangement of ligand binding region;
4. What is the influence of the pocket volume on establishing relationships between protein structure and its ligand/coactivator; and
5. Which residues play pivotal roles in the dynamics communication between AF-2 and the ligand-binding pocket, and how these key residues at crucial positions within the LBD confer kinetic rules for the functional link.

In view of the difficulties in the perturbation dynamics of the AF-2 and the ligand-binding pocket, including the essential interactions involved, molecular dynamics (MD) simulation techniques provide a useful tool to gain insight into the conformational features of AR and the stabilization effect of DHT/SRC2-3(SRC) binding on the structure of AR. Therefore, in this study, we examine four systems for AR LBD interactions with target coactivator SRC and ligand DHT, that is, AR-apo (unbound), DHT·AR, AR·SRC, and DHT·AR·SRC by MD simulations to search for the structural relay between AF-2 and the ligand-binding region, and also to explore which parts in the AR LBD work synergistically, to improve the understanding of the AR transcriptional activity. Our studies confirm a synergism that the coactivator SRC and the androgen DHT exert by mutually induced conformational perturbations in AR-LBD.

METHODS

Structural preparation

The initial crystal structure of DHT·AR·SRC was obtained from the Protein Data Bank (PDB ID: 1t63). For AR-apo, it was built by removing both the crystal DHT and SRC (residues: 919–933) from the 1t63. As for DHT·AR and AR·SRC, the two binary conformations of AR, were generated by removing SRC and DHT from the crystal structure 1t63, respectively.

Hydrogen atoms were added by using the LEAP module in AMBER.¹⁵ All the energy minimization and dy-

namics simulation for proteins were carried out with the FF03 force field.¹⁶ Parameters for DHT were obtained from ANTECHAMBER module using the Generalized Amber force field (GAFF)¹⁷ and the AM1-BCC charge scheme.^{18,19} The starting structures were neutralized with counter ions (Na^+), and were explicitly solvated using TIP3P water²⁰ in a rectangle water box ($87.48 \text{ \AA} \times 77.90 \text{ \AA} \times 87.67 \text{ \AA}$ for AR-*apo*, $87.48 \text{ \AA} \times 77.89 \text{ \AA} \times 87.67 \text{ \AA}$ for DHT-AR, $87.48 \text{ \AA} \times 77.89 \text{ \AA} \times 87.67 \text{ \AA}$ for AR-SRC, and $87.48 \text{ \AA} \times 77.89 \text{ \AA} \times 87.67 \text{ \AA}$ for DHT-AR-SRC), keeping a minimum distance of 12 \AA between the solute and each face of the box. The cutoff distance was kept to 8 \AA to compute the nonbonded interactions. All the simulations were performed under periodic boundary conditions, and long-range electrostatics was treated by using the particle-mesh-Ewald (PME) method.²¹ To remove possible bad contacts, the complexes were energy minimized by a multistep procedure. First, water molecules were allowed to relax, with the rest of the systems kept frozen. Second, all atoms were allowed to move. Energy minimization was then performed with 5000 steepest-descent steps followed by 5000 conjugate-gradient steps. Constant volume dynamics with a cutoff of 8 \AA was chosen. SHAKE²² was turned on for bonds involving hydrogen atoms.

Molecular dynamics

The first step of MDs was to heat up the minimized systems to 300 K at a constant rate of 6 K/ps constraining the protein atoms. The second step consisted of a 50 ps pressure-constant period to raise the density while still keeping the complex atoms constrained. The third step was a 500 ps Langevin dynamics calculation with a collision frequency of 1 ps^{-1} , which was performed for the systems with a 2 fs time step in the NPT ensemble at a constant temperature of 300 K. Finally, the production phase was run for 20 ns, considering that each trajectory is long enough to ensure sufficient sampling of the protein's configuration space and the ligand, that is, allowing the systems to cross the barrier between folded and misfolded free energy basins more than once. Simulations were performed using the Andersen temperature coupling scheme²³ with a time constant of 2 ps. The PME method was always with the default values throughout the simulations. Snapshots were collected from the stable structures during the last 10 ns of the four simulations for analysis (1 snapshot/5 ps).

Cross-correlation analysis

Cross-correlation analysis was applied to correlate motions between any pair of residues in the four AR-related simulations, and the last 10 ns of the production run were selected. The cross-correlation coefficient C_{ij} between atoms i and j , is a measure of the correlated

nature of their atomic fluctuations and was computed as follows

$$C_{ij} = \langle \Delta r_i \times \Delta r_j \rangle / (\langle \Delta r_i \times \Delta r_i \rangle \langle \Delta r_j \times \Delta r_j \rangle)^{1/2} \quad (1)$$

where Δr_i and Δr_j are the displacement vectors for atoms i and j , respectively. The angle brackets denote an average over the trajectory. The value of C_{ij} ranges from -1 to 1 with the correlated (positive) residue pair moving in the same direction, and the anti-correlated (negative) pair moving in the opposite direction.²⁴

Volume calculation

Protein binding site volumes were calculated using the CASTp server (<http://sts-fw.bioengr.uic.edu/castp>).²⁵ The solvent probe radius used for volume calculation was 1.40 \AA . In the calculation of CASTp, pockets that matched the pocket resolved by crystallography were selected, and the volume of the calculated pocket was taken as the volume of the protein binding site.

Principal components analysis

In this study, PCA^{26,27} has been performed to identify and compare the principal modes of motion of the AR, using the four MD structure ensembles, that is, AR-*apo*, DHT-AR, AR-SRC, and DHT-AR-SRC. Global translational and rotational movements during the trajectories were removed by using a least-squares fitting routine. Then the eigenvalues and eigenvectors (C) representing the direction and amplitude of the motion were calculated by diagonalizing the covariance matrix

$$C = \langle XX^T \rangle \quad (2)$$

where $x = r - \langle r \rangle$ represents the protein atomic displacement vectors in the $3N$ dimensional configuration space, N the number of atoms, r an atomic coordinate vector, and the angular brackets represent averages over a MD trajectory. To visualize the motions represented by the eigenvectors, the structures from the ensembles were projected onto each eigenvector of interest and transformed back into Cartesian coordinates. As PCA reduced the dimensionality of the trajectory data, using only the first several principal components we could extract important dynamical features describing collective and overall motions of the four systems.

Energy calculation

Small molecule binding affinity

The binding affinities of DHT to the crystal structure (1t63) and other four models obtained from the average structures of the last 10 ns simulations, that is, AR-*apo*, DHT-AR, AR-SRC, and DHT-AR-SRC, were calculated.

This calculation procedure was based on an empirically derived consensus scoring function that integrated a rapid energy evaluation through the precalculated grids of affinity potentials with the Lamarckian genetic algorithm to search suitable binding positions for DHT on AR.²⁸ The empirical function has the following form:

$$\begin{aligned} \Delta G_{\text{bind}}^{\text{aq}} = & W_{\text{vdW}} \sum_i \sum_j \left(\frac{A_{ij}}{r_{ij}^{12}} - \frac{B_{ij}}{r_{ij}^6} \right) \\ & + W_{\text{hbond}} \sum_i \sum_j E(t) \left(\frac{C_{ij}}{r_{ij}^{12}} - \frac{D_{ij}}{r_{ij}^{10}} \right) \\ & + W_{\text{elec}} \sum_i \sum_j \frac{q_i q_j}{\epsilon r_{ij}} + W_{\text{tor}} N_{\text{tor}} \\ & + W_{\text{sol}} \sum_i \sum_j (S_i V_j + S_j V_i) \exp\left(-r_{ij}^2/2\sigma^2\right) \end{aligned} \quad (3)$$

where W_{vdW} , W_{hbond} , W_{elec} , W_{tor} , and W_{sol} denote the weighting factors of van der Waals, hydrogen bond, electrostatic interactions, torsional term, and desolvation energy of ligands, respectively. The hydrogen bond term has an additional weighting factor, $E(t)$, representing the angle-dependent directionality. A sigmoidal distance-dependent dielectric function was applied in calculating the interatomic electrostatic forces between AR and DHT.²⁹ In the desolvation term, S_i and V_i represent the solvation parameter and the fragmental volume of atom i ,³⁰ respectively. Thirty solutions (poses) for each docked molecule were scored and saved for further analysis.

Protein-protein binding analysis

The coactivator-protein binding analysis was performed using Hex (<http://www.csd.abdn.ac.uk/hex/>) that is interactive graphics for calculating and displaying feasible interacting modes or pairs of proteins.³¹ The average structures of AR-*apo*, DHT-AR, AR-SRC, DHT-AR-SRC as shown above, together with the crystal 1t63 were used as the starting structures of AR, and the crystal SRC fragment from 1t63 was docked into these protein models, respectively. Correlation type and post-processing output for receptor and coactivator were kept based on shape, electrostatic potential, and molecular mechanics (MM) minimization. The calculated total energy (E_{total}) included the shape energy (E_{shape}) and electrostatic energy (E_{force}).³² Five thousand solutions with the lowest energy were generated, and then clustered with an RMSD threshold of 2.0. Other parameters were set as default.

Molecular mechanic Poisson-Boltzmann surface area calculation

To evaluate the energy contributions in the binding interactions of DHT, namely the electrostatic, nonpolar, and configurational entropy components, DHT-AR and

DHT-AR-SRC complexes were subjected to MD simulations and the resulting trajectories were analyzed using the molecular mechanic Poisson-Boltzmann surface area (MM-PBSA) method.³³ All energetic analyses were done using a single trajectory approach, where each complex, protein and DHT snapshots were taken from the snapshots of performed MD trajectories. According to the MM-PBSA method integrated in AMBER 10,³⁴ the binding free energy (ΔG_{bind}) of each system could be conceptually summarized as follows

$$\Delta G_{\text{bind}} = \Delta G_{\text{com}} - (\Delta G_{\text{rec}} + \Delta G_{\text{lig}}) \quad (4)$$

$$\Delta G = \Delta E_{\text{MM}} + \Delta G_{\text{solv}} - T\Delta S \quad (5)$$

in which

$$\Delta E_{\text{MM}} = \Delta E_{\text{bond}} + \Delta E_{\text{angle}} + \Delta E_{\text{torsion}} + \Delta E_{\text{vdw}} + \Delta E_{\text{ele}} \quad (6)$$

$$\Delta G_{\text{solv}} = \Delta G_{\text{PB}} + \Delta G_{\text{SA}} \quad (7)$$

$$\Delta G_{\text{SA}} = \gamma SA + b \quad (8)$$

where G_{com} , G_{rec} , and G_{lig} are the free energies for the complex, receptor, and ligand, respectively.

The free energy (ΔG) can be estimated in terms of the molecular mechanical (MM) gas-phase binding energy (ΔE_{MM}), the solvation free energy (ΔG_{solv}), and the vibrational entropy term ($T\Delta S$) as in Eq. (5). ΔE_{MM} [Eq. (6)] denotes the average molecular mechanics energy contributed by bonded (ΔE_{bond} , ΔE_{angle} , and $\Delta E_{\text{torsion}}$) and nonbonded (ΔE_{vdw} and ΔE_{ele}) terms, and the individual nonbonded contribution of the binding pocket to ligand was further decomposed on a residue basis using MM-PBSA. The solute entropy contribution ($-T\Delta S$) was estimated by normal-mode analysis using the NMODE module in AMBER 10. ΔG_{solv} [Eq. (7)] is the solvation free energy given by polar solvation free energy (ΔG_{PB}) evaluated using the Poisson-Boltzmann equation, and nonpolar contribution to solvation free energy (ΔG_{SA}) from the surface area.³⁵ The electrostatic solvation free energy was calculated using DELPHI^{36,37} software, with low dielectric medium for solute ($\epsilon = 1$) and high dielectric medium for solvent ($\epsilon = 80$). To be consistent with molecular mechanics energy calculation, the partial charges on solute were still taken from the Amber ff03 all atoms force field. A grid spacing of 0.25 Å was employed for the cubic lattice, and 1000 linear iterations were performed. The nonpolar contribution to the solvation free energy of the ligand was estimated from the SASA by using a linear scaling factor of $\gamma = 0.0072 \text{ kcal}/(\text{mol}\cdot\text{Å}^2)$ derived from the Eq. (8). The dielectric interface separating the solute and solvent regions was defined by the solvent-excluded molecular sur-

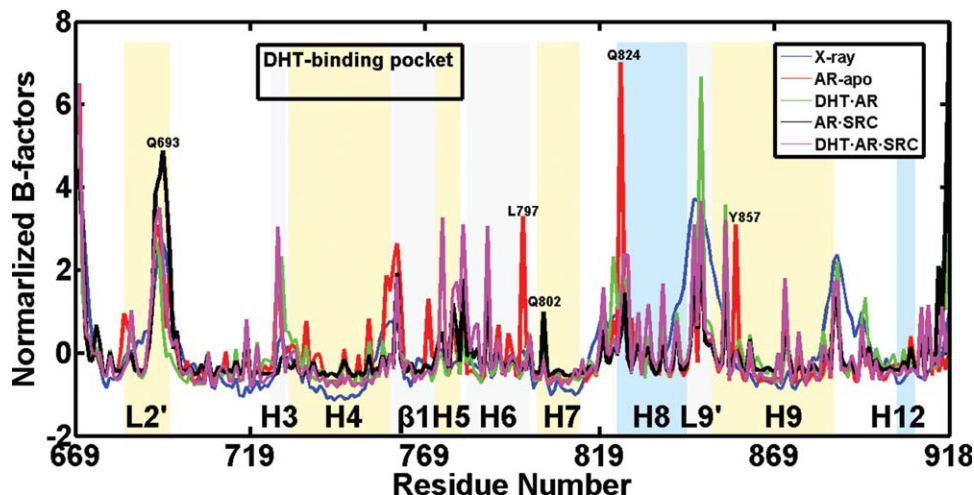


Figure 1

Normalized B-factors plotted for C α atoms of residues in AR-apo (red), DHT-AR (green), AR-SRC (black), DHT-AR-SRC (pink), and 1t63 crystal (blue). The secondary structure elements are indicated: loops 2' and 9' (L2' and L9'), helices 3–9 (H3, H4, H5, H6, H7, H8, and H9), and β -sheet 1 (β 1). The ligand-binding pocket is formed by H3, H4, and H5 whereas the AF-2 groove is formed by helices 3, 4, 5, and 12.

face, obtained with a solvent probe radius of 1.40 Å. Finally, a total of 400 snapshots were extracted from the last 2 ns MD trajectories at a 5 ps interval.

The four systems were first minimized before switching over for normal-mode analysis, using a distance dependent dielectric constant of $\epsilon = 4r$ (r = interatomic distance), in the absence of solvent to mimic solvent screening³⁸ until the convergence criteria of 0.0001 kcal/(mol Å) was achieved. Because normal mode calculation was extremely time-consuming and usually gave an inaccurate estimation for solute entropies, our calculation was only based on the average entropy values computed from 30 snapshots extracted every 5 ps for the last 150 ps.

RESULTS

Structural stability and flexibility

To investigate the fate of AR in the presence of DHT and SRC, a separate 20 ns MD simulation of AR-apo was performed and compared to the data obtained for the DHT-AR, AR-SRC, and DHT-AR-SRC complexes. The root-mean-square deviation (RMSD) of each snapshot from the initial, energy-minimized structure was calculated after alignment based on C α atoms (shown in Supporting Information, Fig. S1). As judged from the convergent RMSD plots, we note that for the monomer, dimer, and trimer systems there is an initial rise in RMSD over the first \sim 6 ns, and stay at this magnitude for up to 20 ns of simulation. Importantly, no sudden shifts are observed in these characteristics. Thus, the structures of the four systems are well described by our models throughout the course of the simulations. RMSD

values fall within reasonable limits throughout the runs, that is, 0.50–1.90 Å in the monomer, dimer, and trimer runs. The overall values of all C α RMSDs for the monomer (1.23 Å) and dimer (1.29 Å for DHT-AR and 1.35 Å for AR-SRC) systems are higher than that for the trimer system (0.99 Å). As can be seen in Figure S1, the AR trajectories over the three simulations escape from the stable level toward a different stable level with an RMSD of \sim 1.70 Å. It is evident that the degree of conformational drift in the ternary simulation is significantly less than in the apo and binary simulations, showing that the presence of either DHT or SRC may stabilize the AR conformation. Overall, this analysis shows that these models are stable in the entire simulations. But it is still unclear whether the presence or absence of DHT/SRC influences the degree of conformational drift of the DHT-binding and AF-2 regions. Therefore, it is a necessity to analyze the motions in more details to extract the key information regarding the structure-function relationship.

The MD simulations also allow one to calculate the B-factors, which are a measure of the flexibility and fluctuations around the average protein structure. In Figure 1, the normalized B-factors of C α atoms are plotted as function of residue index for the four AR-related runs together with the X-ray data (1t63). Examining first the B-factor profile for the DHT-AR-SRC simulation, we see that the overall pattern is close to that observed in the crystallographic B-values. In particular, the peaks in the B-factor profile coincide with the helices between the secondary structure elements. Figure 1 also compares the simulation results of the monomer, dimer, and trimer systems. Helices 6, 8, 9, and loop 9', which lie in the vicinity of the DHT-binding region and contain the

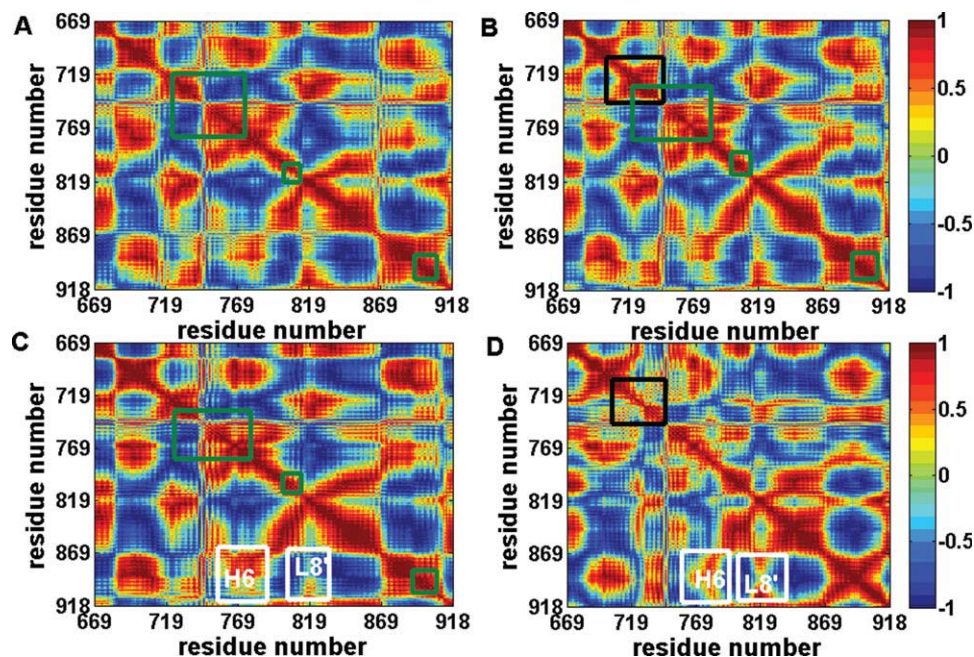


Figure 2

Dynamical cross-correlation maps illustrating the correlation of motion between residues in (A) AR-apo; (B) DHT-AR; (C) AR-SRC; and (D) DHT-AR-SRC. The ligand-binding pocket of AR LBD is formed by the helices 3, 4, 5, β -sheet 1 (residues 724–778), helix 7 (residues 800–812), and helices 11 and 12 (residues 892–908), which are indicated by green rectangles in A, B, and C, respectively. The black frames in B and D show helices 3 and 4 and loop 3' (residues 722–739), whereas the white frames in C and D represent helix 6 and loop 8', respectively. The color bars on the right indicate the extent of the correlation. Residue pairs with a high level of correlated motions are shown in yellow, orange, and red. Anti-correlated motions are represented by the blue and cyan regions. [Color figure can be viewed in the online issue, which is available at wileyonlinelibrary.com.]

residues Trp796, Leu797, Gln824, Lys825, Tyr857, and Gln858, become more mobile in the isolated monomer simulation than the dimeric and trimeric AR (Fig. 1). For AR-SRC, there is a moderate narrowing of the mobility of β -sheet1 and helix 4 compared to the monomer system, also forming part of the DHT-binding region. Other than these changes, higher fluctuations are observed predominantly in the dimeric structure loop 2', being a pronounced region. B-factors of DHT-AR and AR-apo differ mainly in the helices 4, 5, 6, 8, and β -sheet1 which are adjacent to the DHT-binding site, showing that the addition of DHT has produced relatively stable dimeric AR.

Most notably, residues 691–695 (loop 2') and 802–803 (helix 7) near the DHT-binding pocket in the trimer exhibit much lower B-factor values than the same residues in the SRC-bound dimer (Fig. 1). In addition, the trimer system shows a significant mobility of the helix 3 around AF-2 after binding of DHT, indicating that the presence of DHT in the ligand-binding region seems to increase the fluctuation of the AF-2 region. This interesting phenomenon provides evidence of dynamic communication between the two regions in the trimer system. The presence of SRC in the trimer system actually increases the B-factors of the helices 5 and 6 residues. This is in contrast to the DHT-AR system, which exhibits

decreased fluctuations in the DHT-binding region. The mobility of the ligand-binding region in the trimer system is in agreement with the explicitly solvated MD simulations, suggesting that the binding of SRC increases the mobility of the structural conformation around the DHT-binding region.

Cross-correlation analysis

To gain insight into the effects of DHT and SRC on the cooperative dynamics of AR structure, we set out to quantify the correlated motions within AR, as well as to identify those protein regions that move in a concerted fashion depending on the presence of a specific ligand or coactivator. An analysis of the cross-correlation coefficients of pairs of AR residues thus has been performed from the MD simulations. This approach provides a convenient framework to identify the concerted, nonrandom fluctuations^{39,40} as a function of the ligand/coactivator type. Figure 2, the correlation matrix, describes the linear correlation between any pairs of residues as they move around their average positions during dynamics. In this analysis, positive or in-phase correlations are colored in red (strong), orange, and yellow (moderate), whereas negative or out-of-phase correlations are colored in blue (strong) and cyan (moderate).

The correlation matrix for the protein in the AR-apo system shows the existence of both a large number of regions of high correlation and regions of high anti-correlation [Fig. 2(A)]. Interhelix couplings can serve to “transfer information” (e.g., following a conformational transition in one helix) between individual helices. Such interhelix couplings are cross-correlation movements between different helices. For AR-LBD they are found between neighboring helices, loop 2'/helix 2 (686–712), helices 2/3/4 (713–742), helices 4/5/6/ β -sheet1 (747–792), helices 8/9 (829–864), and helices 9/10/11/12/loop 11' (868–908), respectively. These indicate that a good part of the amino acids within several helices in sequence move together but that the direction of motion of the two groups of amino acids is in the opposite sense. This type of motion is characteristic of extensive random movements.

DHT·AR and AR·SRC [Fig. 2(B,C)] are highly similar to the AR-apo map, although both dimer simulations exist slight refluxing. The green rectangles represent movements of residues 724–778 located in helices 3, 4, 5, and β -sheet 1, showing the refluxing of the correlation occur in both the DHT-binding and AF-2 regions in the two maps [Fig. 2(A–C)]. This suggests the existence and propagatable property of a signal of structural interactions between the two regions. As for the DHT·AR·SRC [Fig. 2(D)], most inter-residue motions in each helix have minor correlations, but much larger associations are observed for the inter-helix movements compared with those binary simulations. Such strong correlations may reflect the rigidity of structure of the individual subunits and also the tight coupling of dynamics between them in the protein.

Contribution of ligand binding to subunit interplay

The AR·SRC and DHT·AR·SRC models are compared to understand how the DHT binding influences the interplay between the DHT-binding and AF-2 subunits. In the ternary model, the in-phase movements indicated by red patches in Figure 2(D) are damped compared to those found in the binary form, showing that the conformation of AR is greatly altered by the presence of DHT.⁴¹ At the center region of the ternary map, the helices 4, 5, 6, and 7 and β -sheet1 (residues 759–812) are found to lose their positive cross correlated motions. Some of the greatly weakened correlations correspond to the interhelix pairs forming the ligand binding pocket,⁴² and include the pairs, that is, the lower part of helix 4 (residues 747–758)/helices 5 and 6 (residues 775–784), and β -sheet1 and helices 5 and 6 (residues 764–787)/helices 6 and 7 (residues 789–812). This result clearly indicates that the structural changes occurring upon DHT binding affect mainly the ligand binding pocket, and more importantly, that the movements of the helices and β -sheet are largely independent and there is no direct dynamic coupling

among them. It thus seems that the binding of DHT possibly makes the pocket exhibit a relatively stable conformation, which partly results from the conformation of Arg752 in the ligand binding region since this residue forms a hydrogen bond with DHT in the ternary model. This is also supported by the mutation of Arg752 in the AR ligand-binding region that induces severe androgen insensitivity, enhances the dissociation of bound androgen and causes a loss of the AR stabilization.⁴² This finding might explain from another point of view, why AR degrades intracellularly more quickly with a half-time of ~ 1 h without but 6 h with androgen.⁴³

In addition, as evidenced by the white rectangles in Figure 2(C,D) much higher correlations are observed between loop 8' (residues 814–822)/helices 9, 10, 11, and 12 (residues 863–908), and helix 6 (residues 781–783)/helices 11 and 12 (residues 899–908) in the ternary model. The result shows that that DHT binding promotes the wide-range communication between the neighboring regions, and causes a rearrangement in the AF-2 region.

Contribution of the SRC recruitment to subunit interplay

It is also worth identifying the contribution of the SRC recruitment by comparing the DHT·AR with the DHT·AR·SRC models, since the recruitment of SRC is believed to stabilize the structure of protein while facilitating the ligand binding.⁴⁴ As shown in Figure 2(B), we note that the atomic motions within helices 3 and 4 and loop 3' (residues 722–739, the black rectangle) in the protein convergence of the dimer have well-patterned correlations [the average correlation coefficient (R) is 0.68]. However, after binding to SRC, a weaker correlation ($R = 0.23$) is found within the same region, even with negative correlations between the upper and the lower parts of helix 4 [Fig. 2(D)]. The decreased correlations show the independence of movement of AF-2 region of in the trimer, which might be caused by the recruitment of SRC.

Additionally in the binary model, moderate negative correlation is observed between the lower part of helix 2 (residues 718–721)/ β -sheet1 and helices 5 and 6 (residues 763–798). However, in sharp contrast to the binary form, the lower part of helix 2 gains positive correlation with β -sheet1 and helices 5 and 6 in the ternary model. Since helix 2 lines the top wall of the “Portal” (the DHT-oriented region as shown in Figure 1 formed by helix 4, loop 2', and β -sheet1 in the terminal of DHT-binding pocket), while β -sheet1 and helices 5 and 6 lie at the bottom of the pocket, the collective motions of these helices and β -sheet are proposed to open the Portal region of AR in the ternary model, possibly providing an entry and release channel for DHT. These movements are consistent with the overlapping results of the extreme structures in the PCA analysis for the DHT·AR and DHT·AR·SRC (Fig. S2). In the PCA, we find that loop 2'

moves upward, coupled with the left rotation of helix 5 and the outward movement of helix 6, which interact together to facilitate the pocket opening. This finding can explain at the atomic level the earlier analysis of the androgen dissociation,⁵ where the researchers suggested that the AR LXXLL motif binding to AF-2 region was associated with the dissociation of DHT.

Comparison of the conformational changes by volume and superposition

It is observed that the crystal structure of AR (1t63) overlaps very well with the average structure of the ternary system (Fig. S3), manifesting the reasonability and validity of the dynamics simulations in this study. Intuitively, compared to the monomer, one may expect a larger volume of AR for the dimer due to the expansion of the pocket achieved through DHT uptake, which is confirmed by the evidence that the DHT-binding cavity is 372.1 Å³ in the AR-apo and 753.0 Å³ in the DHT·AR, respectively. However, the fact is that the AR·SRC system has a more collapsed, compact DHT-binding pocket with a volume of 205.6 Å³. As for the DHT·AR·SRC system, this volume is enlarged significantly to 896.4 Å³ because of the corporation of binding of DHT and SRC (all the volumes are calculated from the average geometries of the protein of the last 10 ns simulations).

In the following sections, the average geometries of the protein are further superposed one over the other to evaluate the structure variations due to contribution of the ligand binding and the coactivator recruitment, that is, AR-apo versus DHT·AR, AR-apo versus AR·SRC, AR-apo versus DHT·AR·SRC, and AR·SRC versus DHT·AR·SRC. The pairwise RMSDs of each superposition are 1.78 Å for AR-apo to DHT·AR, 1.87 Å for AR-apo to AR·SRC, 1.13 Å for AR-apo to DHT·AR·SRC, 1.49 Å for AR·SRC to DHT·AR·SRC, 1.87 Å for AR-apo to AR·SRC, as well as 1.40 Å for DHT·AR to DHT·AR·SRC, respectively.

Difference in DHT-binding region

A. AR-apo versus DHT·AR: Figure 3(A) shows the superposition of the average structures of the backbone atoms of the protein for the two models. In the binary model, helix 2 slightly rotates downward with helix 4 shrinking inward relative to the apo model, resulting in expansion of the Portal area of the ligand binding pocket. This can be verified by the Portal surface areas of 7.6 Å² of the monomer (AR-apo) and 16.4 Å² of the dimer (DHT·AR). Further analysis for this variation shows that there are remarkable differences in the orientations of several residues, that is, Gln711, Met749, and Arg752 around the Portal region [Fig. 3(A)]. Compared with the monomer, the right movement (49.10°) of the amide group of Gln711, the downward rotation of the methylthio group of Met749 [the CG-CB torsional angle is 85.90°, which is defined relative to the SD-CG-CB-CA torsion as shown in

Fig. 3(A)], together with the outward dislodgment (47.40°) of the guanidinium group of Arg752, successfully expand the Portal area in the binary model.

In addition, helices 11 and 12, which serve as a core part of the AF-2 region, move averagely downward (2.00 Å) in the DHT·AR compared with the AR-apo [Fig. 3(A) and apo_binary_1.pdb in Supporting Information]. This supports a previous assumption that helix 12 could swing around in the LBD,⁴⁵ since this helix is of remarkable flexibility (Fig. 1) that allows it to move in a large range of motions. These observed motions of helix 12 may be important for the DHT binding, possibly by positioning helix 12 in an appropriate conformation to facilitate the DHT uptake.

B. AR-apo versus DHT·AR·SRC: A superposition of AR-apo to DHT·AR·SRC based on the backbone atoms is displayed in Figure 3(B) and the apo_ternary.pdb (Supporting Information). Helices 2, 6, 9 and the lower part of helix 4 in the monomer have a high degree of overlap with those in the trimer. However, in the AF-2 region, helices 11 and 12 are more close to the center of AF-2 region because of the recruitment of SRC. And helices 7 and 8 and loop 8' move laterally, accompanied by the upward movements of helix 3 and the upper part of helix 4, which increase the room for the AF-2 region to bind to the coactivator SRC. In addition, for the Portal, as shown by the black rectangle in Figure 3(b), two residues, that is, Met749 and Arg752 are found involved in significant changes. Relative to the monomer, the methylthio group of Met749 in the trimer rotates downward of 86.1° to avoid its steric hindrance with the A-ring of DHT, while Arg752 rotates left by 73.1° for its guanidinium group to protrude into the binding pocket, thereby leading to the expansion of the pocket. It is thus implied that the expanded Portal (7.6 Å² for AR-apo and 9.8 Å² for DHT·AR·SRC) caused by the cooperation of the two residues may consequently provide a chance for DHT to escape from the pocket, which is supported by the fluorescence experiments that an increased dissociation of DHT is strongly associated with the levels of coactivator proteins.⁴⁶

C. AR·SRC versus DHT·AR·SRC: Despite the binding of DHT, the superposition between the average AR conformations, obtained from simulations with AR·SRC and DHT·AR·SRC, also shows that the global fold and the main secondary structure elements are highly similar [Fig. 3(CI) and supporting binary_ternary_1.pdb]. The main differences are localized in the DHT-binding pocket. As shown in Figure 3(CII), the pocket inner surface of the binary model (gray) is well embedded in that of the ternary one (purple), showing that the binding pocket is definitely expanded in the ternary system. This observation is consistent with the calculated volume of the pocket in the ternary model that is four times larger than that in the binary one (205.6 Å³ for AR·SRC and 896.4 Å³ for DHT·AR·SRC respectively).

Our simulations also reflect that the conformational changes of Val684, Gln711, Met745, and Arg752 play

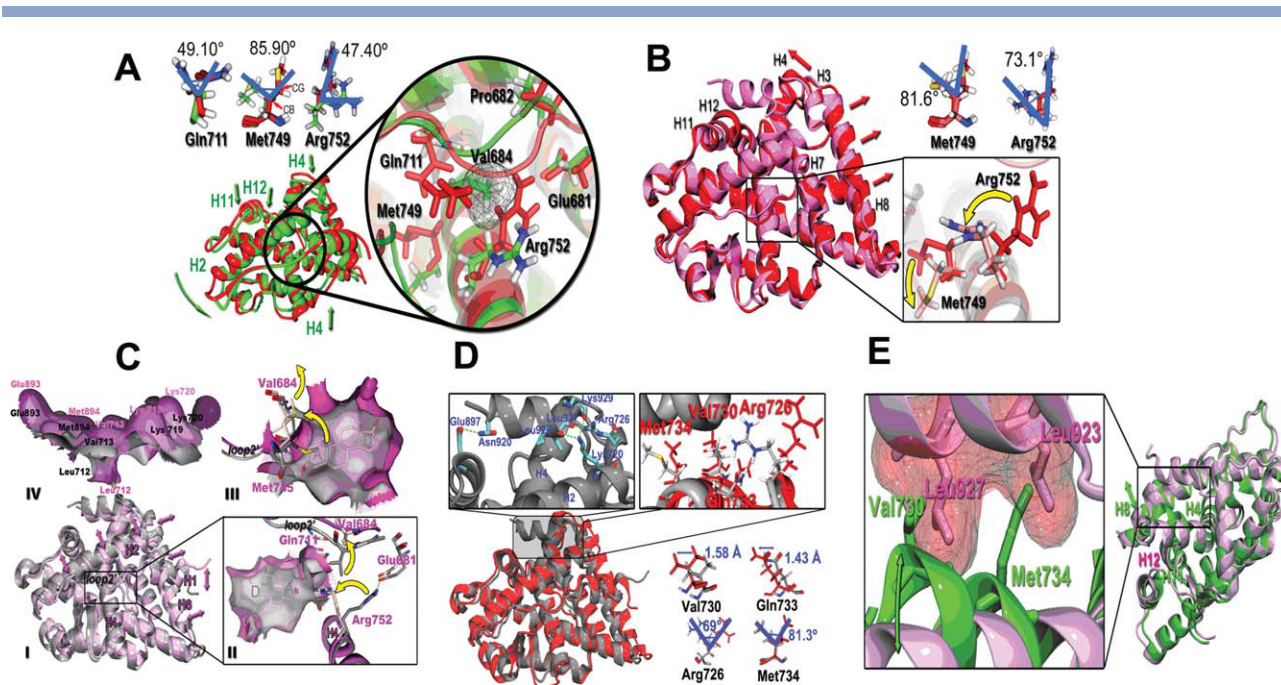


Figure 3

A: Structural superposition of AR-*apo* (red) and DHT-AR (green) models. The projection highlights the Entrance region including Glu681, Pro682, Val684, Gln711, Met749, and Arg752. The gray grid in the center represents the steric effects between Val684 and Arg752 in the dimer. B: Structural superposition of AR-*apo* (red) and DHT-AR-SRC (pink) models. The projection shows the conformational changes of Met749 and Arg752 in the two models, and the yellow arrows are the rotation directions of the two residues in trimer. C: Structural superposition and surface representation of AR-SRC and DHT-AR-SRC models. I: Superposition of the average structures of AR-SRC (gray) and DHT-AR-SRC (purple). II: The projection of the superposed ligand binding pockets in AR-SRC and DHT-AR-SRC. The pocket is in surface representation (gray for AR-SRC and purple for DHT-AR-SRC). The superposition of the pockets in the two models clearly shows the expansion of the binding pocket in the trimer. The ligand DHT in stick format is embedded in the pocket. The labeled “D” represents the hydrophilic terminal, whereas the labeled “A” is the hydrophobic terminal of DHT. III: The back view of Figure 4(II). For clarity, Val684 and Met745 are now shown in stick format. Met745 in the dimer is observed to form strong steric clash with the A-ring of DHT, resulting in a relatively small pocket in the binary model. IV: The superposed AF-2 regions of AR in surface representation (gray for AR-SRC and purple for DHT-AR-SRC). The key residues in this region are labeled, showing that the AF-2 groove is like a cup with the residues like Val713, Lys719, Lys720, Met894, and Glu893 as the rim and Leu712 as the bottom of the cup. D: Structural superposition of AR-*apo* (red) and AR-SRC (gray) systems. The projection on the top-left represents the AF-2 region of AR in the binary model. The projection on the top-right represents the superposed AF-2 regions of AR in the *apo* and binary models, showing the rotation movement of Arg726, Val730, Gln733, and Met734 in dimer. E: Structural superposition of DHT-AR (green) and DHT-AR-SRC (purple) models. The projection denotes the superposed AF-2 regions of the AR including the Leu923, Leu927, Val730, and Met734. The red grids represent the bad contacts between Val730 and Leu927 in trimer, and Met734 in dimer and Leu923 in trimer. [Color figure can be viewed in the online issue, which is available at wileyonlinelibrary.com.]

main roles in expanding the ligand binding pocket. Val684 located in loop 2', like a bolt suspending above the gate undergoes an upward motion (1.00 Å) in the ternary system, which allows a ligand to enter and exit from the binding pocket. For Gln711 [Fig. 3(CII)] and Met745 [Fig. 3(CIII)], both residues in the dimer can form strong steric clash with the A-ring of DHT as shown by the concave in Figure 4(CIII). However, when the amide side chain of Gln711 moves upward with an angle of 60°, coupled with the outward motion of the methylthio group of Met745 (22°) in the trimer, the steric hindrance disappears between the two residues with DHT, which reveals that the structural rearrangement of both residues facilitates the enlargement of the pocket to accommodate DHT. Another interesting find here is that, Arg752 forms a hydrogen bond (H-bond) with Glu681, which bridges loop 2' and helix 4 in AR-SRC [Fig. 4(CII)],

whereas this H-bond is disrupted in the ternary system after binding to DHT. More details will be provided in the subsequent section “Mutual perturbation between the two subunits” of this article.

Additionally, it is considered that the nuclear receptor AF-2 transactivation function is contributed to the surface-exposed hydrophobic cleft involving residues from helices 3, 4, and 12. To understand the unusual contribution of the DHT binding to AF-2, we further compare the structures of AF-2 in complex with/without the SRC [Fig. 3(CIV)]. The surface representation of this region shows the AF-2 groove is like a cup with the residues like Val713, Lys719, Lys720, Met894, and Glu893 as the rim and Leu712 as the bottom of the cup. Compared to the binary model, most rim residues move upward by 1 Å, whereas the bottom (Leu712) extends downward by 0.5 Å, resulting in a deeper cavity of AF-2 region in the

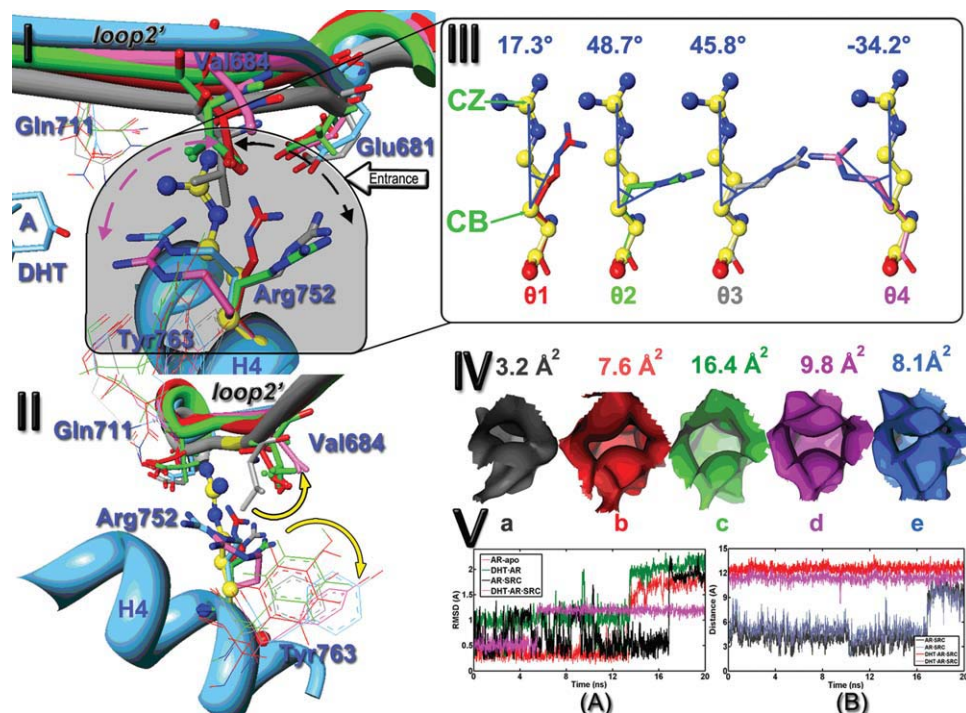


Figure 4

Structural superposition, areas of the Entrance regions and conformations of key residues in AR-apo, DHT-AR, AR-SRC, DHT-AR-SRC, and 1t63 crystal structure models. **I:** The superposed Entrance regions in the five models. The shaded Entrance region shows that Arg752 and Val684 act as gatekeepers to control the entry and exit of DHT. The labeled “Entrance” represents the entry route of DHT. The nitrogen atoms are shown in blue for Arg752 and Val684 in the apo, binary, ternary, and 1t63 crystal models, whereas carbon atoms are in red for AR-apo, in green for DHT-AR, in gray for AR-SRC, in pink for DHT-AR-SRC, and in blue for 1t63 crystal structure, respectively. The native structure of Arg752 is shown in ball and stick form with carbon atoms in yellow (www.ccdc.cam.ac.uk/products/csd/). Tyr763 and Gln711 are shown in solid lines. The pink and black dashed arrows represent the rotation of Arg752 in the different systems compared with its native structure. **II:** A lateral view of Figure 4(I). The yellow arrows show the movement of Val684 and Tyr763 in the different systems. **III:** The angles of rotation of Arg752 in AR-apo (θ_1), DHT-AR (θ_2), AR-SRC (θ_3), and DHT-AR-SRC (θ_4) compared with its native crystal structure represented in ball-and-stick format, respectively. **IV:** Entrance regions of AR in surface representation for the apo, binary, ternary, and crystal simulations. The calculated areas of Entrance region are 3.2 \AA^2 for AR-SRC (a), 7.6 \AA^2 for apo (b), 16.4 \AA^2 for DHT-AR (c), 9.8 \AA^2 for DHT-AR-SRC (d), and 8.1 \AA^2 for the crystal model (e), respectively. **V:** (A) RMSD values (\AA) of Arg752 for the AR-apo (red), DHT-AR (green), AR-SRC (black), and DHT-AR-SRC (pink) models. (B) Hydrogen-bond length of Arg752HH21-Glu681OE1 and Arg752HH22-Glu681OE1 in AR-SRC (blue and black) and DHT-AR-SRC (red and pink) models in the MD. [Color figure can be viewed in the online issue, which is available at wileyonlinelibrary.com.]

ternary model. The striking rearrangement of the AF-2 surface might be caused by the binding of DHT, and to make the AF-2 more appropriate to accommodate the SRC fragment which is composed of a set of bulky hydrophobic amino acids.

Differences in the AF-2 region

A. AR-apo versus AR-SRC: For AR-SRC, the electron donating ability of several electron-rich residues on the SRC fragment is enhanced by the hydrogen bonding of the protons of the residues on the AF-2 region, that is, Leu927-Arg726, Leu926- and Lys929-Lys720, as well as Asn920-Glu897 [Fig. 3(D) and supporting apo_binary_2.pdb]. This probably provides a “push” effect to the ligand binding region, thus compressing the DHT-binding pocket into a more compact cavity, which is supported by the remarkably shrinking volume in the binary

model (205.6 \AA^3) compared with the apo one (372.1 \AA^3). Simultaneously, the AF-2 region is also rearranged due to the recruitment of SRC in a manner that the main chain of Arg726 and Met734 move toward the center of this groove with tilt angles of 69.0° and 81.3° , coupled with the displacement of Val730 and Gln733 by 1.58 and 1.43 \AA , respectively [Fig. 3(D)]. In addition, Figure 2 also shows that the fluctuation of the DHT-binding region in the AR-SRC model is lower than that in the apo model including the lower part of helix 2 (residues 708–721), β -sheet1 (residues 758–771), and helix 5 (residues 772–774), which reveals that the ligand binding pocket is stabilized by the SRC recruitment.

B. DHT-AR versus DHT-AR-SRC: A detailed comparison between DHT-AR and DHT-AR-SRC is performed to gain more understanding of how the SRC recruitment influences the LBD through interactions with the AF-2 region [Fig. 3(E) and supporting binary_ternary_2.pdb].

Hydrogen bonding has been the subject of interest due to its prevalence and importance in the protein-coactivator affinity. In the AF-2 region of the ternary model, H-bonds remain intact at the trajectories simulated as long as 17.0 ns for Lys720HZ1-Leu926O, Lys720HZ1-Lys929O, Lys720HZ2-Leu926O, Lys720HZ2-Lys929O, Lys720HZ3-Leu926O, and Lys720HZ3-Lys929O, although two other H-bonds of Glu897OE1-Lys918HZ2 and Glu897OE1-Lys918HZ3 are seen relatively shorter with the time of 7.0 ns (Supporting Information Fig. S4). The high prevalence together with the strength revealed by the H-bond distance clearly indicate that this set of intermolecular H-bonding is a pincer-like action resembling the closing of a Crab's claw responsible for the recruitment of SRC to the protein. For the ligand binding pocket in the ternary model, helix 2 and loop 2' move upward by ~ 0.5 Å, while helices 5 and 6 move downward by ~ 1.0 Å compared with the binary model, leading to the expansion of the pocket. This suggests that it might be the recruitment of SRC that transmits a concomitant lifting and pulling effect to this cavity and stabilizes it, which is supported by the larger pocket volume of the ternary model (753.0 Å³ for DHT-AR and 896.4 Å³ for DHT-AR-SRC, respectively). This result explains the assumption that the SRC recruitment stabilizes the AR-ligand association, and enhances the overall stability of the receptor.^{2,7}

In addition, bad van der Waals contacts can be observed around the AF-2 region for AR-DHT when it is well overlapped to the ternary model, as shown by the grid balls in Figure 3(E). These bad contacts are displayed between Val730-Leu927 and Met734-Leu923, with the average distance between the residue and its surrounding spherical "neighborhood" < 1.00 Å. The appearance of these contacts further reveals that the residues Val730, Met734 located in the upper part of helix 4 are drawn out to a proper position by SRC to ensure the H-bonding/van der Waals interactions between the four residues. More details will be provided in the following section "Mutual perturbation between the two subunits."

Mutual perturbation between the two subunits

By analyzing superposition of the crystal structure with the average conformations of the four simulations, it is found that the various AR-related modes exhibit a high degree of similarity in their secondary structure elements, especially the core axis helix 4, helix 7, and helix 9 at the bottom of the pocket (Fig. 3). However, several key residues within the active sites still exhibit significant conformational changes, which are found extremely important for the ligand recognition and SRC recruitment, that is, Val684, Arg752, Glu681, Tyr763, and Gln711 (Fig. 4).

Formed by residues Glu681, Pro682, Gly683, and Val684, Loop 2' seems to be an arch suspended over the Portal. In this loop, the bolt-like Val684 (upside), coupled with the opposite Arg752 (downside) in helix 4

serve as two gatekeepers by opening or closing the gate to control the traffic of ligand [Fig. 4(I,II)]. Detailed analysis of the performance of the two gatekeepers will provide us deep understanding of the mechanism of this really interesting physiology.

Arginine contains a 3-carbon aliphatic straight chain, and the distal end of its side chain is capped by a positively charged guanidinium group, which makes it easy to bind to molecules with negative charges. The rotatable, long straight chain leads to arginine with many possible conformers, which could explain why it has the potential to rotate inside or outside of the ligand binding pocket. The flexibility of Arg752 is also supported by its large B-factors in the four systems. The Arg752 in the apo model displays the most significant flexibility (B-factor = 72.86), with relatively lower mobility in other three models, that is, 43.06, 34.39, and 10.51 of B-factor values for DHT-AR, AR-SRC, and DHT-AR-SRC, respectively.

In fact, Arg752 populates four conformations in the four systems: an erection conformation (AR-apo model), two right-rotated closed conformations (DHT-AR and AR-SRC models), and a left-rotated splayed conformation (DHT-AR-SRC model) [Fig. 4(I,II)]. The four conformations are characterized by the self-torsional angles θ_1 , θ_2 , θ_3 , and θ_4 , which are defined as the angles of rotation of Arg752 in the four models compared with its native crystal structure represented in ball-and-stick mode in Figure 4(III) (www.ccdc.cam.ac.uk/products/csd/), respectively. In the AR-apo model, Arg752 is almost straight, similar to its free state, with θ_1 [CZ-CB-CZ as shown in Fig. 4(III)] of 17.3° . Given that the side chain of this residue adopts a conformation close to its native state in vacuum. For the DHT-AR model, the guanidinium end of Arg752 rotates right and points outside of the ligand-binding pocket with θ_2 (CZ-CB-CZ) of 48.7° . Similar to this finding, this residue also adopts a similar orientation in the AR-SRC model with a θ_3 (CZ-CB-CZ) of 45.8° . However in the ternary system, Arg752 drastically rotates left and is embedded in the binding pocket, exhibiting a totally different direction compared with other three models, with θ_4 (CZ-CB-CZ) of -34.2° . And the conformation of Arg752 in the ternary model exhibits the same orientation in the X-ray structure 1t63.

As shown above, in both the DHT-AR and AR-SRC models, the straight side chains of Val684 adopt similar conformations that lie in a staggered, almost vertical direction to helix 4. The residue Val684 directs downward (represented in stick) in the two models, producing a steric barrier in the gate which evidently hinders the entry of the guanidinium group of Arg752 into the pocket.

In the ternary model, after the recruitment of SRC to the AF-2 region, SRC forms several hydrogen bonds with Lys720 and Glu897 in the groove to facilitate the upward movement of helices 2, 3, 4, 11, and 12 (Fig. S4). Simultaneously, the pocket is inflated to approximately one time more than the pocket volume of DHT-AR, which

will help pushing those helices (H2, H3, H4, H11, and H12) closer to the SRC fragment. On the basis of the synergistic effect of DHT and SRC binding, the helix 2 transmits a pulling force to loop 2', leading to the upward movement of Val684 (by ~ 1 Å) [Fig. 3(C,E)]. The movement of Val684 precludes its steric barrier to Arg752 in the ternary model, allowing the counterpart guanidinium end of Arg752 to penetrate into the pocket, consequently triggering the ligand entry/exit route through this channel [Fig. 4(I)].

The above results clearly show the different conformations of Arg752 in the four models, which findings, naturally, raise the question of what cooperative interaction of DHT and SRC binding on the LBD can influence the rotation of Arg752. Figure 4(IV) shows the change of the Portal areas in the four simulations due to the binding of DHT and SRC. Through analyzing the AR-SRC and DHT-AR-SRC models, a negative charged amino acid Glu681 is found involved in the conformational changes of Arg752. Glu681 situates in loop 2', with its end carboxyl group extending downward to the terminal of Arg752 in the binary structure [Fig. 4(I,II)]. The proper distance in space between the two amino acids makes them possible to form hydrogen bonds between each other, with Glu681 as a H-bond donor and Arg752 as a H-bond acceptor. In AR-SRC, although the H-bond length between Glu681 and Arg752 is averagely ~ 5.0 Å, the bond length < 3.5 Å occupies about 20% in the entire simulation time [Fig. 4(VB)], indicative of transient interstrand H-bonding (i.e., helix 4 and loop 2') between the two residues. The high fluctuations of the H-bond length as shown by the distance and RMSD data [Fig. 4(V)] imply that this H-bond is very subtle in its strength, and is easily cleaved under small systematic fluctuations. This phenomenon is consistent with the cross-correlation analysis (Fig. 2), where we identify an evident correlation of motions between Glu681 and Arg752 with R of 0.54 in the AR-SRC model. The interesting feature shows that the two residues cooperate with each other to close the ligand entry channel, thus preventing the DHT from entering the binding pocket. However, in the ternary structure, such a H-bond is definitely broken since the bond length is found about 12 Å for the entire simulated trajectory [Fig. 4(VB)].

In Figure 4(VA), we also plot the RMSD of Arg752 of the apo, binary, and ternary complexes to explore the rotational movement of this residue. In the AR-SRC model, the RMSD over the first 8.3 ns shows a rapid and large fluctuation ranging from 0.2 to 1.4 Å due to the intermittent hydrogen bond between Glu681 and Arg752, finally shifting to what appears to be a new stationary state around the value of 2 Å. While for the DHT-AR, since no hydrogen bond is formed between Glu681 and Arg752, a relatively high mobility of Arg752 is observed (RMSD = ~ 1.1 Å) over the first 6.5 ns, and then the RMSD increases to

~ 2.0 Å and remains stable to the end of simulation. As for the DHT-AR-SRC model, its RMSD remains ~ 0.5 Å during the first 2.8 ns, and jumps to reasonable plateau around 1.2 Å, indicating that the hydrogen bonds are formed between DHT and Arg752.

Despite the above insightful observations of Arg752 for the AR-SRC and DHT-AR-SRC models, structural and functional basis for Arg752 rotation in the DHT-AR model is still unclear. In DHT-AR, loop 2' arranged crosswise with the helix 4 is in close proximity to the β -sheet1 forming one lateral side of the ligand-binding pocket. Val684 in loop 2' and Try763 in β -sheet1 act as two vertical door bolts that meet in the middle of the Portal region when closed [Fig. 4(II)]. Relative to the ternary model, the methyl group of Val684 in AR-DHT lies in a lower position, thus has a shorter distance with the phenolic group of Try763, that is, 3.2 Å for DHT-AR (the closed state) and 11.0 Å (the open state) for DHT-AR-SRC [Fig. 4(II)]. Since the attractive force increases with the decreased distance between two electric charges, there should be a stronger attractive force between the hydrophobic residues Val684 and Try763 in the binary model compared with the ternary one. The hydrophobic interaction thus seems to keep a massive media in the Portal region to prevent the entry of the hydrophilic residue Arg752, consequently pushing its side chain to orientate the outside of the pocket in the binary model.

Energy calculation

Ligand binding affinity

As a complement to the structural data discussed above, estimates of the binding free energy between ligand and AR in the various binding modes have been performed. To discern whether the presence of SRC gives rise to a higher binding avidity for AR with the ligand, the receptor is treated as rigid and only the ligand's flexibility is considered in the score-based binding process. Under such circumstances, only the ligand configurations can vary among different pose parameters to yield an ideal pose, while not allowing induced fit in the protein. Implicit in this study is the idea that we compare the stable conformations of AR in the crystal, apo, binary, and ternary systems to explore the ligand-protein interactions with/without the recruitment of SRC. For space reasons, only the main points of our analysis are outlined below.

We notice a significant consistency of the docking scores when comparing the redocking result of the crystal complex to that of the DHT-AR-SRC model (Fig. S5). Closer inspection of the ternary model reveals that the ligand DHT is well packed in the ligand-binding pocket, and the interactions of DHT with the protein [Fig. S(5D)] are totally consistent with that of the crystal model. This observation logically corresponds to the perfect matches of the ternary and crystal complexes, and

demonstrates the reliability and validity of the scoring system and the ternary model. Further, we find that the structures with optimum pocket volume yield high total cores (7.60, 7.69, and 7.48 for the crystal, DHT-AR, and DHT-AR-SRC models, respectively), whereas the structures with compact volumes have much lower scores (-22.60 for the AR-apo and -12.22 for the AR-SRC).

For the DHT-AR model [Fig. S(5B)], it differs from the ternary one by lacking of the coactivator recruitment, particularly by lossing of the hydrogen bonding contribution between DHT and Arg752. Intuitively, since it is proposed that the Arg752-related hydrogen bond plays an important role in the DHT binding, the binding pose of DHT should have unsuitable protein interpenetration, and thus yielding a much low score. However, actually a high score is assigned to the binary model, which reason, we speculate, is that the ligand is prone to respond in an expected binding pocket with relatively large size based on the underlying physiological state. The details of this will be discussed in section “Mutual perturbation between the two subunits.”

For the AR-apo model [Fig. S(5A)], the binding is coupled to an unfavorable conformational change in the active site of the protein. The A ring of DHT has a strong steric clash with residues Gln711 and Met749 in the Portal region despite a hydrogen bonding of DHT with Asn705. This achieved inappropriate binding pose explains the lowest score yielded for the free model. As for the AR-SRC model [Fig. S(5C)], it is clear that DHT can not penetrate into the ligand binding pocket due to its compact volume. Thus the ligand can only reside outside of the pocket, indicating also an unsuitable binding mode. Therefore, we conclude that the AR protein and the key residues are not likely displaced in a compensatory affect to accommodate the ligand in the binding pocket without the recruitment of SRC.

Analyzing for the above apo, binary, and ternary models suggests that the size of pocket volume and the conformations of key residues play pivotal roles in accommodating the ligand binding. The detailed structural properties found in this study thus provide insight into DHT-AR binding structures, and estimate the contribution of SRC recruitment to the ligand binding pocket. This result is in consistent with the earlier dynamics analysis, which suggests that the conformational change of the DHT-binding region is driven by the SRC, that is, induced-fit-type of binding occurs, resulting in accommodation of the ligand binding.

Coactivator binding energy

As mentioned above, the conformational changes of the pocket and the related residues have emerged as key factors that influence the recruitment of SRC to the protein AR. To illustrate the effects of DHT binding, we also consider the binding of the protein and the coactivator into their biologi-

Table I
Interaction Energies in the Docked Complexes

System	Conformation	E_{total}	E_{shape}	E_{force}	E_{shape}/E_{total}	E_{force}/E_{total}
X-ray	1	-644.60	-477.30	-167.30	0.74	0.26
DHT-AR-SRC	1	-536.40	-327.80	-208.60	0.61	0.39
AR-SRC	2	-514.60	-275.50	-239.10	0.54	0.46
AR-apo	6	-477.10	-266.90	-210.20	0.56	0.44
DHT-AR	5	-468.30	-323.10	-145.20	0.69	0.31

All energies are in kJ/mol.

cally relevant complex structure. In this protein-protein binding, the receptor and the coactivator are both considered to be conformational rigid. The aim is to explore the influence of stable conformations of AR from the crystal, apo, binary, and ternary models to the binding of DHT.

Models are first filtered based on the distance constraints that force the contacts between the specificity-determining residues Leu927, Lys929, Asp930 with Lys720 across the interface, respectively, and the lowest energy structures are selected. Then the conformations in a parallel orientation as the crystal SRC (1t63) are adopted from those low-energy structures, which are most favored for the SRC recruitment. On the basis of the obtained models, the difference of each blind binding is investigated to provide a basis for interpreting the contribution of DHT to the conformational arrangement of AR. The results are shown in Supporting Information, Figure S6 and Table I.

As shown in Table I, the order of the efficiency is observed as the crystal model (most efficient) > DHT-AR-SRC > AR-SRC > AR-apo > DHT-AR (least efficient). The ternary binding mode is highly consistent with the crystal mode for the coactivator recruitment despite of the energy difference, that is, -536.40 kJ/mol for the former and -644.60 kJ/mol for the latter. Such affinity discrepancy should be attributed to the structural difference of SRC in the two models since the coactivator SRC occupies a portion of the AF-2 groove in the ternary model [Fig. S(6D)], which is consistent with the crystal model.

For the AR-apo model [Fig. S(6A)], interaction mismatch is observed that the SRC binding to AR is proximately parallel to helix 2 in this model. At the AF-2 interface of the AR-SRC model [Fig. S(6C)], the side chains of residues Lys720 and Ile898 [Fig. S(6C)] are tightly inter-digitated with the corresponding residues of the SRC peptide, that is, Asp928, Lys929, Asp930, and Asn920, causing severe steric clashes among them. However, AR contacting DHT [Fig. S(6B)] shows the lowest energy mainly due to an unfavorable steric interaction between Lys720 and Asp930, which suggests that the DHT binding is not the unique factor that influences the conformational change of the AF-2 region. These observations reveal that the DHT-induced conformational changes, that is, the structural rearrangement of AF-2 region, facilitate the binding of SRC complexes to the

AR, which are in accordance with the cross correlation and dynamic analysis of the DHT binding in sections “Cross-correlation analysis” and “Comparison of the conformational changes by volume and superposition.”

Table I further presents the ratio of E_{shape} (energy content of the protein) and E_{force} (binding energy of ligand) to E_{total} ($E_{\text{force}} + E_{\text{shape}}$), respectively. As expected, only including the electrostatic interaction term (E_{force}) in the correlation ($E_{\text{force}}/E_{\text{total}}$) seems not to influence the rank of the binding energies. In contrast, the shape-only blind binding solution ($E_{\text{shape}}/E_{\text{total}}$) function ranks the various geometries stemmed from the five models with sufficient accuracy, showing the scoring of the crystal and DHT·AR models as the global maximum (0.74 for the x-ray model and 0.69 for the DHT·AR model). This verifies the importance of the shape complementarity score (E_{shape}) in the binding energy predication, which suggests that the conformational rearrangement of AF-2 region is the key point for the structured protein–protein interactions, and also proves the contribution of DHT from another aspect.

MM-PBSA

The above energy analysis could be used as good indicators of how the conformational changes in different systems are influenced by the binding of DHT and SRC. It is still important to search for a powerful tool for investigating both the energetics and structural implications of the interaction of AR with DHT (i.e., DHT·AR and DHT·AR·SRC systems) in the presence of solvent and thermal fluctuations. MM-PBSA methodology is highly suitable as it can be implemented on a standard MD simulation. It is also highly insightful as it provides the various components of the binding free energy, including the energy due to Coulombic and van der Waals interactions, electrostatics and nonpolar components of the solvation free energy, and the entropy.³¹ Table II summarizes the MM/PBSA-calculated binding free energies. The consistency between the predicted (−19.71 kcal/mol for the DHT·AR and −19.92 kcal/mol for the DHT·AR·SRC) and experimental binding free energy [−12.72 (Ref. 47) kcal/mol for the DHT·AR and −14.69 (Ref. 48) kcal/mol for the DHT·AR·SRC] shows that the method applied here is reliable and the obtained data can be further analyzed. When compared to DHT·AR, DHT·AR·SRC is mainly attributed to the electrostatic potential energy (ΔE_{ele} , −15.90 kcal/mol for the DHT·AR and −21.94 kcal/mol for the DHT·AR·SRC) and the electrostatic contributions to the solvation free energy (ΔG_{PB} , 28.53 kcal/mol for the DHT·AR and 35.44 kcal/mol for the DHT·AR·SRC). The MM/PBSA results suggest that a crucial factor affecting the binding affinity is to achieve optimal molecular mechanics and van der Waals interaction between the ligand and the protein active site.

Closer inspection reveals that the recruitment of SRC results in a non-negligible change in the electrostatic

Table II

Binding Free Energy and Other Energy Terms to ΔG_{bind} for DHT·AR and DHT·AR·SRC Complexes

Contribution	DHT·AR		DHT·AR·SRC	
	Mean (kcal/mol)	Standard deviation	Mean (kcal/mol)	Standard deviation
ΔE_{ele}	−15.90	3.76	−21.94	2.70
ΔE_{vdw}	−47.10	2.41	−46.23	2.18
ΔE_{MM}	−63.00	3.25	−68.17	2.96
ΔG_{SA}	−5.14	0.07	−5.14	0.11
ΔG_{PB}	28.53	3.34	35.44	2.01
ΔG_{GB}	23.28	3.82	28.21	1.77
$\Delta E_{\text{ele}} + \Delta G_{\text{PB}}$	12.63	2.86	13.50	2.57
$T\Delta S$	−19.90	3.37	−17.95	6.28
ΔG_{bind} (calculated)	−19.71	3.5	−19.92	6.3
ΔG_{bind} (predicted)	−12.72		−14.69	

ΔE_{ele} , electrostatic potential energy; ΔE_{vdw} , van der Waals potential energy; ΔE_{MM} , sum of molecular mechanics (MM) energies of the molecules, and can be further split into contributions from electrostatic (ΔE_{ele}) and van der Waals (ΔE_{vdw}) energies; $\Delta E_{\text{MM}} = \Delta E_{\text{ele}} + \Delta E_{\text{vdw}}$; ΔG_{SA} , nonpolar contributions to solvation free energy; ΔG_{PB} , electrostatic contributions to the solvation free energy calculated with Poisson–Boltzmann equation; ΔG_{GB} , electrostatic contributions to the solvation free energy calculated with generalized Born equation; $\Delta E_{\text{ele}} + \Delta G_{\text{PB}}$, sum of the electrostatic solvation free energy and MM electrostatic energy; $T\Delta S$, change in the calculated entropic contribution to the free energy of binding; ΔG_{bind} , change in the calculated free energy of binding; $\Delta G_{\text{bind}}(\text{exp})$, change in the experimentally determined free energy of binding; $\Delta G_{\text{bind}} = \Delta E_{\text{MM}} + \Delta G_{\text{PB}} + \Delta G_{\text{SA}} T\Delta S$.

potential energy (ΔE_{ele}), nearly 6 kcal/mol, which accounts for the electrostatic interactions between the protein and the peptides that are responsible for large distance molecular recognition.⁴⁹ This change is likely due to the hydrogen bonding as mentioned in section “Differences in the AF-2 region” that is introduced as a result of the SRC recruitment in the AF-2 region. The calculations reveal no change in the nonpolar component of the free energy of solvation (ΔG_{SA}) for the DHT·AR (−5.14 kcal/mol) compared with the DHT·AR·SRC (−5.14 kcal/mol). Despite the slightly favorable contributions from nonpolar effects ($\Delta E_{\text{vdw}} + \Delta G_{\text{SA}}$) for the binary system, the electrostatic contributions as a result of the binding of SRC play a significant role in stabilizing the AR protein, mainly due to the Coulombic interactions (ΔE_{ele}). The increase in the free binding energy due to ΔE_{ele} is compensated by a decrease in the desolvation energy (ΔG_{PB}), which might be the result of the recruitment of SRC. The calculated ΔG_{bind} , −19.71 kcal/mol for the dimer is slightly less than −19.92 kcal/mol for the trimer (Table II), which also indicates that the AR bound with SRC is more suitable to bind to the ligand.

To elucidate the key residues in the DHT-binding region of AR and the most favorable interaction modes, the binding free energy decomposition is performed (Fig. 5). As shown in Figure 5, compared with the ternary model, the binding affinities of some key residues Leu704, Trp741, Met742, Met780, Ile 899 are decreased by more than 0.15 kcal/mol in the dimer. The only reason is that the SRC recruitment facilitates the ligand binding to the pocket, further supporting the above qualitative analysis for the binary and ternary systems.

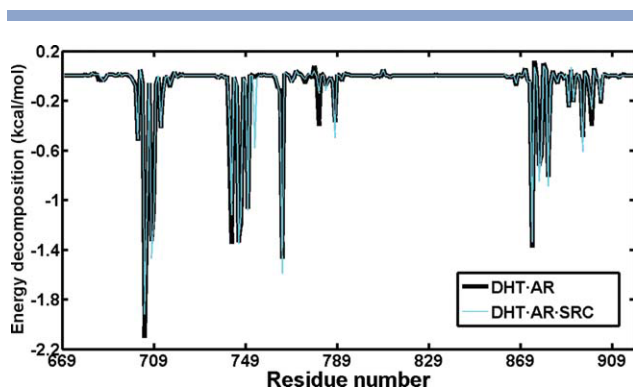


Figure 5

Energy decomposition of the total interaction energy for DHT-AR (black) and DHT-AR-SRC (cyan) models. [Color figure can be viewed in the online issue, which is available at wileyonlinelibrary.com.]

In the ternary structure, Arg752 forms an H-bond with O3-ketone of DHT with the bond length of 2.85 Å and a high occupancy of 71%. However, this Arg752 only contributes about -0.58 kcal/mol and amounts for 2.5% to the total binding affinity for the ternary model. This result shows that this residue does not play a decisive role in the ligand binding, which is consistent with the result in Section “Ligand binding affinity” that the DHT-AR model still yields a high score without the hydrogen bonding contribution of Arg752. This finding supports a previous proposal that this residue could act as a “mouse trap,” which allows a repositioning of the DHT in the pocket.⁵⁰ The displacement of DHT (~ 0.9 Å) appears to decrease the distance between this ligand with the lateral side of the binding cavity, which is significantly pronounced in the visual inspection of the superposed average structures of the two systems. This observation is also reflected by an increasing in $\Delta\Delta G$ (>0.14 kcal/mol) of residues Leu707, Phe764, Met787, Phe876, and Met895 lining in the DHT-binding cavity (Fig. 5). The decomposition analysis of binding affinity of the two systems thus provides us with complementary information about the mechanism by how the SRC finally affects the structures of AR and thus enhancing the binding of DHT.

DISCUSSION

As mentioned above, the C-terminal LBD is a critical part of AR modular structures. It harbors a ligand-binding cavity and a hormone-dependent AF-2 region. The binding pocket formed is strictly confined within the lower half of the LBD. AF-2 is a hydrophobic surface of LBD that lies contiguous to the ligand binding pocket and is structurally dependent on the bound ligand.² Clearly, the two regions of AR do not function independently, but rather act in concert with each other and with other proteins during the androgen activation of transcription. Currently, research has focused on the structural and functional properties of

the binding cavity and the AF-2 region.^{2,5} However, the mechanism of mutual functional interference between the two different binding sites still remains unclear. Complementary to experimental work such as point mutation studies or binding affinity measurements,^{4,47} computer simulations can provide valuable and testable information for exploring the functional link between the two regions. In this study, we have obtained the dynamics processes of the DHT and SRC bindings to AR, as well as the thermodynamic properties involved in these processes with molecular modeling, dynamics simulations and thermodynamic analysis, and thus can gain some insights into the dynamic relationship between DHT and SRC at the atomic level.

As illustrated in Figure 6, the event of the DHT binding to AR follows a conformational change of AF-2 region [1, 4]. A conserved SRC motif subsequently binds to the AF-2 groove in this dimer to facilitate the binding of DHT [8]. On the basis of the ligand binding pathway, we propose a mutual communication between the DHT-binding

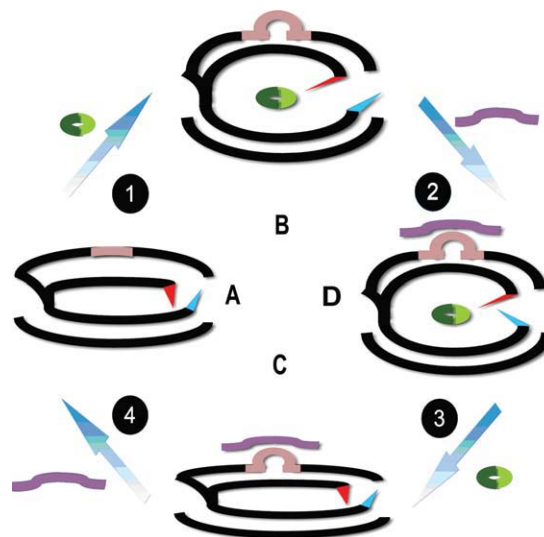


Figure 6

Proposed mechanism of the binding pathway of DHT and SRC and the structural interplay between the ligand-binding pocket and the AF-2 region in the AR. The AR LBD and SRC are drawn vividly as an eye (black) and an eyebrow (purple), respectively, and DHT as eyeballs (green). The black and light greens are hydrophobic and hydrophilic terminals of DHT, respectively. The red triangle represents Val684, and the blue Arg752. A–D represent the AR-*apo*, DHT-AR, AR-SRC, and DHT-AR-SRC, respectively. A: Val684 and Arg752 are approximately vertical to loop 2' and helix 4, respectively, blocking the entry route of DHT. B: The upward movement of Val684 and the right rotation of Arg752 open the Entrance region of the ligand binding pocket to facilitate the entry of DHT. Subsequently, the ligand binding expands the pocket and results in the rearrangement of the AF-2 region. C: The escape of DHT from the Entrance region causes to collapse of the pocket. D: The recruitment of SRC acts as a hand to grasp and pull the AF-2 region, leading to a more enlarged pocket and the left rotation of Arg752. Step 1, the ligand enters the pocket; Step 2, the SRC binds to the AF-2 region; Step 3, the escape of ligand leads to a compact pocket; and Step 4, the loss of SRC to prepare for a new circle. [Color figure can be viewed in the online issue, which is available at wileyonlinelibrary.com.]

and the AF-2 regions, which expands the ligand binding pocket to assist the entry and exit of DHT. This mechanism is consistent with the role of DHT as a modulator, reshaping the LBD surface with concomitant effects on coactivator association,⁴⁷ and also the function of the SRC recruitment in inhibiting the androgen response to intervene the AR activity *in vivo*.⁴⁸

In an inactive state [Fig. 6(A)], Val684 (the red triangle), located in the loop 2' and in the proximity of the Portal region, is almost vertical to loop 2'. Similarly, Arg752 (the blue triangle), located opposite to the Val684, is approximately perpendicular to helix 4. The combination of the two residues clearly blocks the entry route of the ligand. Characterized by the enclosed nature⁵¹ and the compact state⁵² of the ligand binding pocket, AR reveals a considerably lower degree of correlation between the DHT-binding and AF-2 region motions [Fig. 2(A)].

It is generally accepted that the transition from the AR-apo state to the DHT-bound complex is kinetically fast. To furnish rapid, efficient transition from one conformation into another, a cooperative mechanism is necessary, because AR must be reliably converted into its expanded state to accommodate the DHT. Here in Step 1 (Fig. 6), we suggest a cooperative opening mechanism, in which the rotations of Val684 and Arg752 in the Portal play major roles [Fig. 6(B)]. According to the model, once the DHT is binding, with the rapid and repeated push-and-open movements as mentioned in section "Difference in DHT-binding region," the volume of the ligand binding pocket is enlarged with purpose to accommodate the ligand. As the conformation of the pocket is rearranged, the lifting of loop 2' (~1 Å) and the shrinking of helix 4 enable the upward movement of Val684 (~1 Å), together with the right side rotation of Arg752 orientated outside the pocket [Fig. 6(B)]. The observed motions assist the partial expansion of the Portal region [Figs. 3(A) and 4(IV)]. To further confirm the expanded Portal state, a probe of 1.4 Å in radius was used to roll around the van der Waals surface of the residues in the ligand binding region for the AR-apo and the DHT-AR models [Figs. 4(IV) and S7]. In the ternary model, it is clearly found that there is an open Portal region surrounded by residues Glu681, Val684, Gln711, Arg752, and Tyr763, which allows the ligand to cross [Fig. 4(I,II)]. However, the region involved in the ligand binding, which is opposite to the Portal region, is blocked by the electrostatic interactions between the residues of opposite charges such as the Leu701 and Thr877, Phe891 and Thr877, as well as Leu701 and Trp741 as shown in supporting Figure S7. This observation explains why the ligand could not enter the pocket via this region directed by the D-ring of DHT (Fig. S7).

However, it is still not clear which terminal of the DHT first enters the ligand binding pocket from the Portal region. To address this question, we consider the effect of hydrophobic attraction between the Portal region and

DHT, which is an important driving force for biological structures and is responsible for protein-small molecule interactions.⁵³ The blue surface (at the lower part of Fig. S7) suggests the existence of a hydrophobic Portal region formed by several hydrophobic amino acids, such as the Val684, Val685, Val746, Phe747, and Trp751. Clearly, this hydrophobic ligand binding pocket is more favorable to draw those ligands with higher hydrophobicity.⁵⁴ Interestingly, DHT is a highly hydrophobic molecule with a log *P* value of 4.07, with a significant difference in hydrophobicity observed in its two ends, that is, the D-ring (log *P* = 1.43, the black green terminal) and the A-ring (log *P* = 0.7, the light green terminal) terminals (Fig. 6). Clearly, the more hydrophobic terminal, the ring D of DHT, therefore prefers to first enter the binding pocket due to its larger hydrophobic attraction with the Portal region than the ring A [Fig. 6(B)].

Following the ligand binding, in Step 2, AR translocates to the nucleus and associates with the coactivators GRIP-1 (the glucocorticoid receptor interacting protein 1, also termed SRC2) [Fig. 6(D)] and histone acetylase p300/CBP (CREB-binding protein) in subnuclear foci.⁵⁵ Our data show that the ligand binding leads to a series of movements of the LBD, such as the outward movement of helices 2, the upward motion of helix 3 and the downward movement of helix 12 neighbored in space. The motions of AR appear to form a more extended, diffuse AF-2 region to prepare for the recruitment of the SRC.⁵⁶ Upon the SRC recruitment, loop 2' and helix 2 move upward to cause the lifting motion of Val684, coupling with the left-rotation of Arg752 stemmed from the decreased hydrophobic force between the Val684 in Loop 2' and the Trp763 in β-sheet1 as mentioned in section "Mutual perturbation between the two subunits." The displacement of loop 2' and helix 2 suggests that AR undergoes a transition to an extended state upon the binding of its partner (SRC). This implies that the expanded pocket is favored over the dissociation of DHT. As a consequence, the recruitment of SRC controls the escape of DHT from the ligand binding pocket, which explains why a mutation in the FXXLF motif or Glu895 in AF-2 resulting in an increased dissociation of the androgen bound to AR.⁵

Subsequently (Step 3), the side chain of Arg752 swings out of the binding pocket to push the ligand away from the binding pocket and thus intensifies the collapse of the AR LBD that already occurs in this region. Such an alteration results in a more compact receptor and energetically unstable state as shown in Figures 4(IV) and 6(C). At the last step (Step 4), the resulting complex leads to the necessary escape of SRC from AR, showing a cycling of the coactivator on and off the androgen-regulated promoters. And finally, a new circle of AR transcription is initiated, which is consistent with the observation that the same receptor molecule may be able to conduct up to four rounds of transcription.

In this section, a model for the mutual perturbation between the ligand binding pocket and the AF-2 region has been proposed, revealing that the agonist binding to the hormone-binding site perturbs the structure of the pocket and distorts the AF-2 surface. While the recruitment of the coactivator SRC stabilizes the AR-ligand association and promotes the release of DHT from the DHT-binding cavity. Our analysis therefore shows, for the first time, the mutually induced conformational perturbations in the AR ligand-binding region using MDs simulations. To further elucidate the communication between the androgen and coactivator, experimental studies are hoped to be carried out in future.

CONCLUSION

In the present work, four 20 ns MDs simulations of AR in the presence of DHT and SRC were performed. On the basis of the obtained trajectories, we report that the DHT binding can provide inherent structural stability to the ligand binding domain, and arrange the conformation of the AF-2 region to improve the SRC coactivator recruitment. And the SRC coactivator binding facilitates the locking of DHT in the ligand-binding pocket mainly through the side chain movements of Arg752 and Val684, and provides a novel entry and escape route for DHT. In addition, MM-PBSA was used to analyze the detailed interaction and binding free energies in the DHT·AR and DHT·AR·SRC complexes. The results from free energy decomposition indicate that the polar solvation free energy (ΔG_{PB}) provides the driving force for the binding of DHT with AR and AR·SRC. Through the residue interaction analysis, we identify that for the DHT·AR simulation, residues Leu704, Trp741, Met742, Met780, and Ile899 contribute obviously. Although for the DHT·AR·SRC simulation, residues with high affinity include the Leu707, Phe764, Met787, Phe876, and Met895. The above information provides some insights for the structure-based design or discovery of drugs in androgen deprivation therapy and will be useful for human beings to fight against prostate cancer due to the association of AR activity in prostate cancer with SRC/p160 coactivators.

REFERENCES

1. Nettles KW, Greene GL. Ligand control of coregulator recruitment to nuclear receptors. *Annu Rev Physiol* 2005;67:309–333.
2. He B, Gampe RT, Jr, Kole AJ, Hnat AT, Stanley TB, An G, Stewart EL, Kalman RI, Minges JT, Wilson EM. Structural basis for androgen receptor interdomain and coactivator interactions suggests a transition in nuclear receptor activation function dominance. *Mol Cell* 2004;16:425–438.
3. Xu X, Yang W, Li Y, Wang Y. Discovery of estrogen receptor modulators: a review of virtual screening and SAR efforts. *Expert Opin Drug Discovery* 2010; 5:21–31.

4. Taplin M. Drug insight: role of the androgen receptor in the development and progression of prostate cancer. *Oncology* 2007;4:236–244.
5. Askew EB, Gampe RT, Stanley TB, Faggart JL, Wilson EM. Modulation of androgen receptor activation function 2 by testosterone and dihydrotestosterone. *J Biol Chem* 2007;282:25801–25816.
6. Gregory CW, He B, Johnson RT, Ford OH, Mohler JL, French FS, Wilson EM. A mechanism for androgen receptor-mediated prostate cancer recurrence after androgen deprivation therapy. *Cancer Res* 2001;61:4315–4319.
7. He B, Gampe RT, Faggart JL, Minges JT, French FS, Wilson EM. Probing the functional link between androgen receptor coactivator and ligand-binding sites in prostate cancer and androgen insensitivity. *J Biol Chem* 2006;281:6648–6663.
8. Danielian PS, White R, Lees JA, Parker MG. Identification of a conserved region required for hormone dependent transcriptional activation by steroid hormone receptors. *EMBO J* 1992; 11:1025–1033.
9. Powell SM, Christiaens V, Voulgaraki D, Waxman J, Claessens F, Bevan CL. Mechanisms of androgen receptor signalling via steroid receptor coactivator-1 in prostate. *Endocr Relat Cancer* 2004;11: 117–130.
10. Lee HJ, Chang C. Recent advances in androgen receptor action. *Cell Mol Life Sci* 2003;60:1613–1622.
11. Feng W, Ribeiro RC, Wagner RL, Nguyen H, Apriletti JW, Fletterick RJ, Baxter JD, Kushner PJ, West BL. Hormone-dependent coactivator binding to a hydrophobic cleft on nuclear receptors. *Science* 1998;280:1747–1749.
12. Moras D, Gronemeyer H. The nuclear receptor ligand-binding domain: structure and function. *Curr Opin Cell Biol* 1998;10:384–391.
13. Shiau AK, Barstad D, Radek JT, Meyers MJ, Nettles KW, Katzenellenbogen BS, Katzenellenbogen JA, Agard DA, Greene GL. Structural characterization of a subtype-selective ligand reveals a novel mode of estrogen receptor antagonism. *Nat Struct Biol* 2002;9:359–364.
14. Wilson EM. Functional Motifs of the Androgen Receptor. *Androgen Action in Prostate Cancer* 2009;3:241–267.
15. Case DA, Darden TA, Cheatham TE, Simmerling CL, Wang J, Duke RE, Luo R, Merz KM, Wang B, Pearlman DA, Crowley M, Brozell S, Tsui V, Gohlke H, Mongan J, Hornak V, Cui G, Beroza P, Schafmeister C, Kollman PA. AMBER 10. San Francisco, CA: University of California; 2008.
16. Duan Y, Wu C, Chowdhury S, Lee MC, Xiong G, Zhang W, Yang R, Cieplak P, Luo R, Lee TA. A point-charge force field for molecular mechanics simulations of proteins based on condensed-phase quantum mechanical calculations. *J Comput Chem* 2003;24:1999–2012.
17. Wang J, Wolf RM, Caldwell JW, Kollman PA, Case D. Development and testing of a general amber force field. *J Am Chem Soc* 2004;25:1157–1174.
18. Jakalian A, Bush BL, Jack DB, Bayly CI. Fast, efficient generation of high-quality atomic charges. AM1-BCC model: I. Method. *J Comput Chem* 2000;21:132–146.
19. Jakalian A, Jack DB, Bayly CI. Fast, efficient generation of high-quality atomic charges. AM1-BCC model: II. Parameterization and validation. *J Comput Chem* 2002;23:1623–1641.
20. Jorgensen WL, Chandrasekhar J, Madura J, Impey RW, Klein ML. Comparison of simple potential functions for simulating liquid water. *J Chem Phys* 1983;79:926–935.
21. Darden T, York D, Pederson L. Particle mesh Ewald: an N^* log (N) method for computing Ewald sums. *J Chem Phys* 1993;98:10089–10092.
22. Ryckaert JP, Cicotti G, Berendsen HJC. Numerical integration of the Cartesian equations of motion of a system with constraints: molecular dynamics of n-alkanes. *J Comput Phys* 1977;23: 327–341.
23. Andrea TA, Swope WC, Andersen HC. The role of long range forces in determining the structure and properties of liquid water. *J Chem Phys* 1983;79:4576–4584.

24. Ichiye T, Karplus M. Collective motions in proteins: a covariance analysis of atomic fluctuations in molecular dynamics and normal mode simulations. *Proteins* 1991;11:205–217.
25. Dundas J, Ouyang Z, Tseng J, Binkowski A, Turpaz Y, Liang J. CASTp: computed atlas of surface topography of proteins with structural and topographical mapping of functionally annotated residues. *Nucleic Acids Res* 2006;34:116–118.
26. Yamaguchi H, Aalten DMV, Pinak M, Furukawa A, Osman R. Essential dynamics of DNA containing a cis-syn cyclobutane thymine dimer lesion. *Nucleic Acids Res* 1998;26:1939–1946.
27. Kitao A, Hayward S, Go N. Energy landscape of a native protein: jumping-among-minima model. *Proteins* 1998;33:425–437.
28. Morris GM, Goodsell DS, Halliday RS, Huey R, Hart W, Belew RK, Olson AJ. Automated docking using a Lamarckian genetic algorithm and an empirical binding free energy function. *J Comput Chem* 1998;19:1639–1662.
29. Mehler EL, Solmajer T. Electrostatic effects in proteins: comparison of dielectric and charge models. *Protein Eng* 1991;4:903–910.
30. Stouten PFW, Frommel C, Nakamura H, Sander C. An effective solvation term based on atomic occupancies for use in protein simulations. *Mol Simul* 1993;10:97–120.
31. Kollman PA, Massova I, Reyes C, Kuhn B, Huo S, Chong L, Lee M, Lee T, Duan Y, Wang W, Donini O, Cieplak P, Srinivasan J, Case DA, Cheatham TE. Calculating structures and free energies of complex molecules: combining molecular mechanics and continuum models. *Acc Chem Res* 2000;33:889–897.
32. Ritchie DW, Kemp GJ. Protein docking using spherical polar Fourier correlations. *Proteins* 2000;39:178–194.
33. Kuhn B, Donini O, Huo S, Wang JM, Kollman PA. MM-PBSA applied to computer-assisted ligand design. In: Reddy MR, Erion MD, editors. *Free energy calculations in rational drug design*. New York: Kluwer Academic/Plenum Publishers; 2001. pp 243–251.
34. Case DA, Cheatham TE, Darden T, Gohlke H, Luo R, Merz KM, Jr, Onufriev A, Simmerling C, Wang B, Woods RJ. The Amber biomolecular simulation programs. *J Comput Chem* 2005;26:1668–1688.
35. Sitkoff D, Sharp KA, Honig B. Accurate calculation of hydration free energies using macroscopic solvent models. *J Phys Chem* 1994;98:1978–1988.
36. Rocchia W, Sridharan S, Nicholls A, Alexov E, Chiabrera A, Honig B. Rapid grid-based construction of the molecular surface and the use of induced surface charge to calculate reaction field energies: Applications to the molecular systems and geometric objects. *J Comput Chem* 2002;23:128–137.
37. Honig B, Sharp K, Yang AS. Macroscopic models of aqueous solutions: biological and chemical applications. *J Phys Chem* 1993;97:1101–1109.
38. Chong LT, Duan Y, Wang L, Massova I, Kollman PA. Molecular dynamics and free-energy calculations applied to affinity maturation in antibody 48G7. *Proc Natl Acad Sci USA* 1999;96:14330–14335.
39. Ichiye T, Karplus M. Collective motions in proteins: a covariance analysis of atomic fluctuations in molecular dynamics and normal mode simulations. *Proteins* 1991;11:205–217.
40. Bradley MJ, Chivers PT, Baker NA. Molecular dynamics simulation of the Escherichia coli NikR protein: equilibrium conformational fluctuations reveal interdomain allosteric communication pathways. *J Mol Biol* 2008;378:1155–1173.
41. Matias PM, Donner P, Coelho R, Thomaz M, Peixoto C, Macedo S, Otto N, Joschko S, Scholz P, Wegg A, Basler S, Schafer M, Egner U, Carrondo MA. Structural evidence for ligand specificity in the binding domain of the human androgen receptor. *J Biol Chem* 2000;275:26164–26171.
42. Yarbrough WG, Quarmby VE, Simental JA, Joseph DR, Sar M, Lubahn DB, Olsen KL, French FS, Wilson EM. A single base mutation in the androgen receptor gene causes androgen insensitivity in the testicular feminized rat. *J Biol Chem* 1990;265:8893–8900.
43. Kempainen JA, Lane MV, Sar M, Wilson EM. A single base mutation in the androgen receptor gene causes androgen insensitivity in the testicular feminized rat. Androgen receptor phosphorylation, turnover, nuclear transport, and transcriptional activation. Specificity for steroids and antihormones. *J Biol Chem* 1992;267:968–974.
44. Heinlein CA, Chang C. Androgen receptor (AR) coregulators: an overview. *Endocr Rev* 2002;23:175–200.
45. Duff J, McEwan IJ. Mutation of histidine 874 in the androgen receptor ligand-binding domain leads to promiscuous ligand activation and altered p160 coactivator interactions. *Mol Endocrinol* 2005;19: 2943–2954.
46. Burd CJ, Morey LM, Knudsen KE. Androgen receptor corepressors and prostate cancer. *Endocr Relat Cancer* 2006;13:979–994.
47. Estébanez-Perpiñá E, Moore JMR, Mar E, Delgado-Rodriguez E, Nguyen P, Baxter JD, Buehrer BM, Webb P, Fletterick RJ, Guy RK. The molecular mechanisms of coactivator utilization in ligand-dependent transactivation by the androgen receptor. *J Biol Chem* 2005; 280:8060–8068.
48. Kempainen JA, Langley E, Wong C, Bobseine K, Kelce W, Wilson E. Distinguishing androgen receptor agonists and antagonists: distinct mechanisms of activation by medroxyprogesterone acetate and dihydrotestosterone. *Mol Endocr* 1999;13:440–454.
49. Obiol-Pardo C, Rubio-Martinez J. Comparative evaluation of MMPBSA and XSCORE to compute binding free energy in XIAP-peptide complexes. *J Chem Inf Model* 2007;47:134–142.
50. Buchanan G, Yang M, Harris HM, Nahm HS, Han G, Moore N, Bentel JM, Matusik RJ, Horsfall DJ, Marshall VR, Greenberg NM, Tilley WD. Mutations at the boundary of the hinge and ligand binding domain of the androgen receptor confer increased transactivation function. *Mol Endocrinol* 2001;15:46–56.
51. Lonard DM, O'Malley BW. The expanding cosmos of nuclear receptor coactivators. *Cell* 2006;125:411–414.
52. Chang CY, Abdo J, Hartney T, McDonnell DP. Development of peptide antagonists for the androgen receptor using combinatorial peptide phage display. *Mol Endocrinol* 2005;19:2478–2490.
53. Huang DM, Chandler D. The Hydrophobic Effect and the Influence of Solute-Solvent Attractions. *J Phys Chem B* 2002;106:2047–2053.
54. Chandler D. Interfaces and the driving force of hydrophobic assembly. *Nature* 2005;437:9640–9647.
55. Black BE, Vitto MJ, Gioli D, Spencer A, Afshar N, Conaway MR, Weber MJ, Paschal BM. Transient, ligand-dependent arrest of the androgen receptor in subnuclear foci alters phosphorylation and coactivator interactions. *Mol Endocrinol* 2004;18:834–850.
56. Gao W, Bohl CE, Dalton JT. Chemistry and structural biology of androgen receptor. *Chem Rev* 2005;105:3352–3370.